NeuroImage: Clinical 32 (2021) 102882

Contents lists available at ScienceDirect

NeuroImage: Clinical

journal homepage: www.elsevier.com/locate/ynicl

"Aerobic glycolytic imaging" of human gliomas using combined pH-, oxygen-, and perfusion-weighted magnetic resonance imaging

Akifumi Hagiwara [a,b,c], Jingwen Yao [a,b,d], Catalina Raymond [a,b], Nicholas S. Cho [a,b,d,e], Richard Everson [f], Kunal Patel [f], Danielle H. Morrow [g], Brandon R. Desousa [g], Sergey Mareninov [h], Saewon Chun [i], David A. Nathanson [g], William H. Yong [h], Gafita Andrei [g], Ajit S. Divakaruni [g], Noriko Salamon [b], Whitney B. Pope [b], Phioanh L. Nghiemphu [i,j], Linda M. Liau [f], Timothy F. Cloughesy [i,j], Benjamin M. Ellingson [a,b,d,i,k,*]

[a] UCLA Brain Tumor Imaging Laboratory (BTIL), Center for Computer Vision and Imaging Biomarkers, University of California, Los Angeles, Los Angeles, CA, USA
[b] Department of Radiological Sciences, David Geffen School of Medicine, University of California, Los Angeles, Los Angeles, CA, USA
[c] Department of Radiology, Juntendo University School of Medicine, Tokyo, Japan
[d] Department of Bioengineering, Henry Samueli School of Engineering and Applied Science, University of California Los Angeles, Los Angeles, CA, USA
[e] Medical Scientist Training Program, David Geffen School of Medicine, University of California Los Angeles, Los Angeles, CA, USA
[f] Department of Neurosurgery, David Geffen School of Medicine, University of California, Los Angeles, Los Angeles, CA, USA
[g] Department of Molecular and Medical Pharmacology, David Geffen School of Medicine, University of California Los Angeles, Los Angeles, CA, USA
[h] Department of Pathology, David Geffen School of Medicine, University of California Los Angeles, Los Angeles, CA, USA
[i] UCLA Neuro-Oncology Program, University of California, Los Angeles, Los Angeles, CA, USA
[j] Department of Neurology, David Geffen School of Medicine, University of California Los Angeles, Los Angeles, CA, USA
[k] Department of Psychiatry and Biobehavioral Sciences, David Geffen School of Medicine, University of California Los Angeles, Los Angeles, CA, USA

ARTICLE INFO

Keywords:
Aerobic glycolysis
amine CEST
^{18}FDG-PET
Glioblasoma
Glioma
IDH

ABSTRACT

Purpose: To quantify abnormal metabolism of diffuse gliomas using "aerobic glycolytic imaging" and investigate its biological correlation.

Methods: All subjects underwent a pH-weighted amine chemical exchange saturation transfer spin-and-gradient-echo echoplanar imaging (CEST-SAGE-EPI) and dynamic susceptibility contrast perfusion MRI. Relative oxygen extraction fraction (rOEF) was estimated as the ratio of reversible transverse relaxation rate R_2' to normalized relative cerebral blood volume. An aerobic glycolytic index (AGI) was derived by the ratio of pH-weighted image contrast (MTR_{asym} at 3.0 ppm) to rOEF. AGI was compared between different tumor types (N = 51, 30 IDH mutant and 21 IDH wild type). Metabolic MR parameters were correlated with ^{18}F-FDG uptake (N = 8, IDH wild-type glioblastoma), expression of key glycolytic proteins using immunohistochemistry (N = 38 samples, 21 from IDH mutant and 17 from IDH wild type), and bioenergetics analysis on purified tumor cells (N = 7, IDH wild-type high grade).

Results: AGI was significantly lower in IDH mutant than wild-type gliomas (0.48 ± 0.48 vs. 0.70 ± 0.48; $P = 0.03$). AGI was strongly correlated with ^{18}F-FDG uptake both in non-enhancing tumor (Spearman, $\rho = 0.81$; $P = 0.01$) and enhancing tumor ($\rho = 0.81$; $P = 0.01$). AGI was significantly correlated with glucose transporter 3 ($\rho = 0.71$; $P = 0.004$) and hexokinase 2 ($\rho = 0.73$; $P = 0.003$) in IDH wild-type glioma, and monocarboxylate transporter 1 ($\rho = 0.59$; $P = 0.009$) in IDH mutant glioma. Additionally, a significant correlation was found between AGI derived from bioenergetics analysis and that estimated from MRI ($\rho = 0.79$; $P = 0.04$).

Conclusion: AGI derived from molecular MRI was correlated with glucose uptake (^{18}F-FDG and glucose transporter 3/hexokinase 2) and cellular AGI in IDH wild-type gliomas, whereas AGI in IDH mutant gliomas appeared associated with monocarboxylate transporter density.

* Corresponding author at: UCLA Brain Tumor Imaging Laboratory (BTIL), Biomedical Physics, Psychiatry, and Bioengineering, Departments of Radiological Sciences and Psychiatry, David Geffen School of Medicine, University of California, Los Angeles, 924 Westwood Blvd., Suite 615, Los Angeles, CA 90024, USA.
E-mail address: bellingson@mednet.ucla.edu (B.M. Ellingson).

https://doi.org/10.1016/j.nicl.2021.102882
Received 17 June 2021; Received in revised form 10 November 2021; Accepted 11 November 2021
Available online 12 November 2021

1. Introduction

Metabolic reprogramming is a hallmark of cancer. Glycolysis is often augmented in malignant cells, even in the presence of abundant oxygen (Venneti and Thompson, 2017), in a process known as aerobic glycolysis or the 'Warburg effect.' This abnormal metabolism results in a substantial decrease in local extracellular pH due to increased production of lactic acid and other factors (Gatenby and Gillies, 2004). Increased extracellular acidity potentially contributes to tumor malignancy by inducing mutagenesis, invasion, angiogenesis, immunosuppression, chemoresistance, and promotion of glioma stem cells (Corbet and Feron, 2017; Morita et al., 1992). This phenomenon is in part mediated by hypoxic induction of hypoxia-inducible factor 1-alpha (HIF1α) (Brat et al., 2004), leading to overexpression of glycolysis-related proteins/enzymes, namely, glucose transporter, hexokinase, monocarboxylate transporter, and lactate dehydrogenase, thereby accelerating glycolysis (Fig. 1) (Venneti and Thompson, 2017). These prinicples in general apply to malignant gliomas (Venneti and Thompson, 2017). However, given inter-tumoral heterogeneity in glioma, these molecular processes vary. For example, in IDH mutant glioma (Koivunen et al., 2012), HIF1α response to hypoxia is blunted, resulting in lower expression of HIF1α related genes and shift of the glucose metabolism to oxidative phosphorylation (Chesnelong et al., 2014). Nevertheless, metabolic perterbations remain an important area of study in the biology of IDH mutant and wild-type gliomas.

Molecular imaging is a promising method for non-invasively investigating the metabolic characteristics of different types of tumors and differentiating tumor progression from treatment effect (Wu et al., 2016). Recently, a pH- and oxygen-sensitive molecular imaging technique using amine chemical exchange saturation transfer spin-and-gradient-echo echoplanar imaging (CEST-SAGE-EPI) was introduced as a tool to explore tumor acidity and hypoxia simultaneously in human gliomas (Harris et al., 2018). Amine CEST exhibits sensitivity to tissue pH, along with other factors, through quantification of pH-dependent chemical exchange between amine protons on amino acids and bulk water (Sun et al., 2010). Further, the reversible transverse relaxation rate R_2', which is sensitive to local deoxyhemoglobin concentration and hence tissue hypoxia (Fujita et al., 2003), can also be obtained using the multi-echo readout available using CEST-SAGE-EPI and can provide value into oxygen utilization (Harris et al., 2018). However, oxygen extraction is not completely echoed by measures of R_2', as local oxygen extraction can be influenced by underlying blood volume. Even though ^{15}O PET and ^{17}O MRI can specifically detect oxygen consumption, they require radioactive tracers and stable isotopes, respectively (Atkinson and Thulborn, 2010; Lebrun-Grandie et al., 1983; Niesporek et al., 2018). We hypothesize a combination of the above-mentioned CEST-SAGE-EPI and perfusion imaging can be used to quantify the degree of aerobic glycolysis. Specifically, we theorize that an estimate of the relative oxygen extraction fraction (rOEF) can be quantified as the ratio of R_2' to relative cerebral blood volume (rCBV) from perfusion imaging (Toth et al., 2013). Thus, an "aerobic glycolytic index," or AGI, can then be derived as the ratio of tumor acidity, measured by amine CEST, to rOEF, assuming that aerobic glycolysis is reflected by production of lactate under inefficient use of oxygen.

The current study aims to demonstrate the association between AGI and glycolytic function in human gliomas. Using four approaches, we investigate (I) the difference in AGI between different tumor and tissue types; (II) the association between AGI and glucose utilization using ^{18}F-fluorodeoxyglucose (FDG) PET; (III) the correlation between AGI and immunohistochemistry expression of key proteins or enzymes involved in aerobic glycolysis including HIF1α, glucose transporter 3, hexokinase 2, monocarboxylate transporter 1, and lactate dehydrogenase A, from

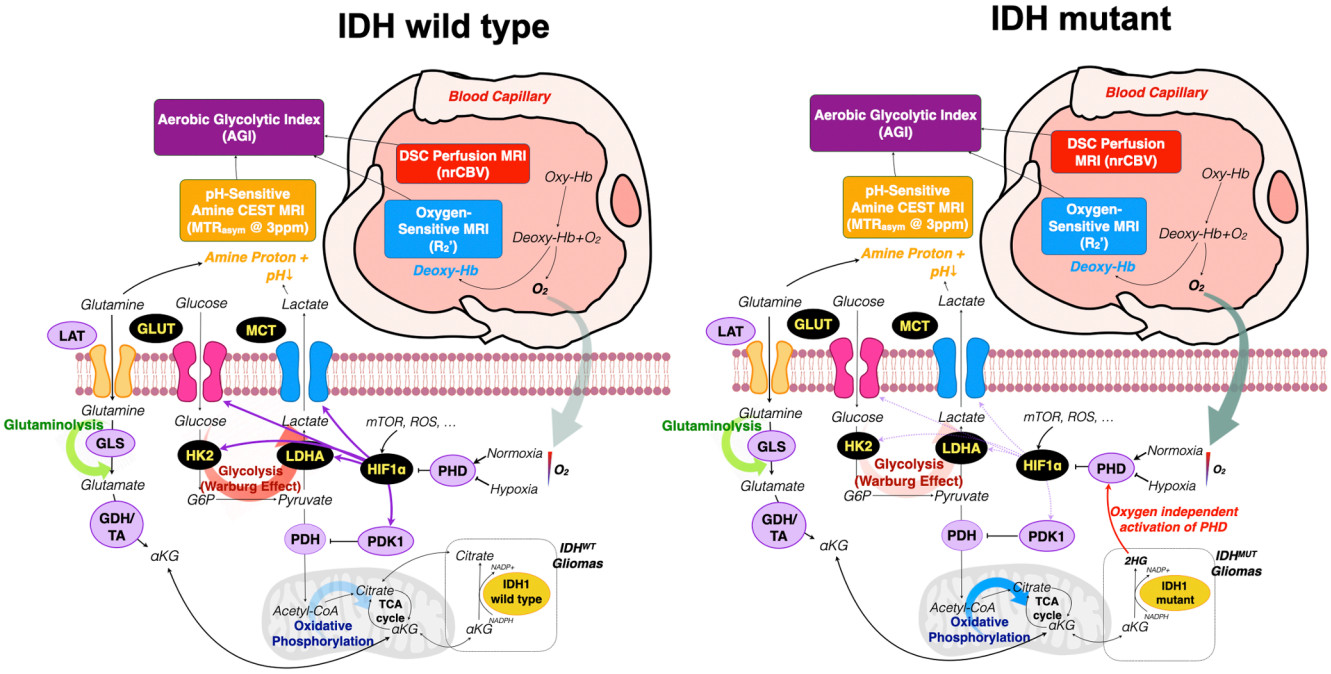

Fig. 1. Schematic overview of metabolic pathway in IDH wild-type and mutant gliomas. Similar to other malignant tumors, IDH wild-type glioma is characterized by a high level of aerobic glycolysis (Warburg effect). Hypoxia induces upregulation of HIF1α, leading to overexpression of glycolysis-related proteins/enzymes, namely, GLUT, HK2, MCT, and LDHA, thereby accelerating glycolysis. On the other hand, HIF1α response to hypoxia is blunted in IDH mutant glioma, shifting the metabolism to oxidative phosphorylation. In this study, the extent of aerobic glycolysis was estimated by pH- and oxygen-sensitive imaging combined with perfusion imaging. The proteins/enzymes investigated in our study are labeled in black. Notably, MTR_{asym} at 3.0 ppm increases not only in accordance with decrease in pH but also with increase in glutamine related to tumor activity. 2HG = 2-hydroxyglutarate, aKG = alpha-ketoglutarate, acetyl-CoA = acetyl coenzyme A, G6P = glucose-6-phosphate, GDH = glutamate dehydrogenase, GLS = glutaminase, GLUT = glucose transporter, HK2 = hexokinase 2, LAT = L-amino acid transporter, LDHA = lactic dehydrogenase A, MCT = monocarboxylate transporter, mTOR = mammalian target of rapamycin, PDH = pyruvate dehydrogenase, PDK1 = pyruvate dehydrogenase kinase 1, ROS = reactive oxygen species, TA = transaminase, TCA cycle = tricarboxylic acid cycle.

image-guided biopsy specimens; and (IV) the relationship between AGI and measurements derived from extracellular flux bioenergetic analysis (Wu et al., 2007) of cultured cells obtained from resected tumor tissue.

2. Materials and methods

In order to characterize the association between AGI and glycolytic function in human gliomas, we performed four separate experiments: Study I compared AGI between IDH mutant and wild-type, and low-grade and high-grade gliomas, and between different tissue types; Study II investigated the correlations between AGI and glucose uptake using ^{18}F-FDG PET; Study III examined the association between AGI and immunohistochemistry staining of critical proteins or enzymes related to aerobic glycolysis, namely, HIF1α, glucose transporter 3, hexokinase 2, monocarboxylate transporter 1, and lactate dehydrogenase A, from image-guided biopsy samples; and Study IV explored the correlation between AGI and measurements derived from extracellular flux bioenergetic analysis of cultured cells acquired from resected glioma tissue.

2.1. Patient population

This study was conducted from April 2015 to May 2018 with institutional review board approval (IRB# 14–001261; 10–000655). Written informed consent was acquired from all participants prior to study-related procedures. All de-identified patient information was stored on a secure research database. This study included 4 distinct patient populations. Table 1 shows the characteristics of these patients. Overlap in patients included: 8 and 3 patients in population I were also in population III and IV, respectively. Forty-four subjects were also included in a previous study that reported the metabolic features of diffuse gliomas by using CEST-EPI and CEST-SAGE-EPI without perfusion imaging (Yao et al., 2019). IDH mutation status was confirmed by genomic sequencing analysis using immunohistochemistry and/or polymerase chain reaction as previously described (Lai et al., 2011).

Table 1
Patient demographics.

Study I	All patients	IDH mutant	IDH wild type
No. of patients*	51	30	21
Median age [range] (y)	52 [21–90]	40.5 [22–78]	59 [21–90]
Sex male/female	38/13	20/10	18/3
WHO grade (II/III/IV)	19/18/14	17/11/2	2/7/12
Scanner Prisma/Skyra	31/20	19/11	12/9
Study II	**All patients**	**IDH mutant**	**IDH wild type**
No. of patients**	8	–	8
Median age [range] (y)	60 [50–72]	–	60 [50–72]
Sex male/female	1/7	–	1/7
WHO grade (II/III/IV)	0/0/8	–	0/0/8
Scanner Prisma/Skyra	3/5	–	3/5
Study III	**All patients**	**IDH mutant**	**IDH wild type**
No. of patients*** (on/off treatment)	15 (2/13)	8 (1/7)	7 (1/6)
Median age [range] (y)	47 [29–62]	42.5 [29–49]	59 [44–62]
Sex male/female	10/5	4/4	6/1
WHO grade (II/III/IV)	5/5/5	4/3/1	1/2/4
Scanner Prisma/Skyra	9/6	5/3	4/3
Study IV	**All patients**	**IDH mutant**	**IDH wild type**
No. of patients (on/off treatment)	7 (3/4)	–	7 (3/4)
Median age [range] (y)	59 [51–68]	–	59 [51–68]
Sex male/female	6/1	–	6/1
WHO grade (II/III/IV)	0/1/6	–	0/1/6
Scanner Prisma/Skyra	3/4	–	3/4

* All patients in Study I were treatment-naïve or had been off any treatment for more than 2 years.
**All patients in Study II had recurrent IDH wild-type glioblastomas at time of MRI
*** Patients prior to any treatment or who had been off any treatment for more than 2 years were considered to be off treatment. Patients who were either on active treatment or recently off treatment at the time of MRI scan were considered on treatment.

Study II utilized baseline, pretreatment imaging data acquired as part of a prospective study to evaluate the metabolic treatment effect of osimertinib (epidermal growth factor receptor tyrosine kinase inhibitor, ClinicalTrials.gov # NCT03732352) in patients with recurrent IDH wild-type glioblastoma. Patient population II included 8 patients (median age, 60 years; range 50–72 years). All subjects were scanned with CEST-SAGE-EPI, perfusion imaging, and ^{18}F-FDG PET at recurrence, prior to any treatment, for the current study.

Patient population III included 15 patients with histologically confirmed diffuse gliomas (median age, 47 years; range 29–62 years). A total of 38 tissue samples (21 from IDH mutant and 17 from IDH wild type) were acquired.

Patient population IV included 7 patients (median age, 59 years; range 51–68 years) with high-grade (WHO grade III and IV) IDH wild-type gliomas. The contrast-enhancing portions of tumor were biopsied and cultured.

2.2. MR acquisition

All patients were scanned with CEST-SAGE-EPI, dynamic susceptibility contrast (DSC) perfusion MRI, and anatomical imaging on 3-T scanners (Prisma or Skyra, Siemens Healthcare, Erlangen, Germany). Anatomical imaging was performed according to the standardized brain tumor imaging protocol (Ellingson et al., 2015). CEST imaging was performed prior to contrast administration. The CEST-SAGE-EPI sequence consisted of a saturation pulse train of three 100-ms Gaussian pulses with the peak amplitude B_1 of 6 μT and a SAGE-EPI readout consisting of 2 gradient echoes with echo times of 14.0 and 34.1 ms, one asymmetric spin-echo with a TE of 58.0 ms, and one spin-echo with echo time of 92.4 ms. The other acquisition parameters were: repetition time greater than 10000 ms; field of view = 217 × 240 mm; matrix size = 116 × 128; number of slices = 25; slice thickness = 4.0 mm with no interslice gap; partial Fourier encoding = 6/8, generalized autocalibrating partially parallel acquisition (GRAPPA) = 3; and bandwidth = 1628 Hz/pixel. A total of 29 z-spectral points was acquired at offset frequency from − 3.5 ppm to − 2.5 ppm; from − 0.3 ppm to + 0.3 ppm; and from + 2.5 ppm to + 3.5 ppm, all with respect to the water proton resonance frequency. An additional reference (S0) scan was obtained with 4 averages using the identical parameters without saturation pulses. The other details of the sequence are described elsewhere (Harris et al., 2018). The total acquisition time of CEST-SAGE-EPI was 7 min 30 s, benchmarked on a 3-T Prisma MR scanner (Software Version VE11C).

For DSC-perfusion MRI, a total dose of 0.1 mmol/kg of gadolinium diethylenetriaminepentacetate (Magnevist; Bayer HealthCare Pharmaceuticals, Wayne, New Jersey) was administered with 0.025 mmol/kg for the preload dosage to mitigate T1-based leakage contamination and the remaining 0.075 mmol/kg for dynamic bolus administration. The preload dose and the start of baseline DSC-MRI was separated for 2 min. The acquisition parameters were: echo time/repetition time = 17/2250–2000 ms; flip angle = 35–90°; field of view = 240 × 240 mm; matrix size = 128 × 128; slice thickness = 4–5 mm with no interslice gap; number of slices = 25–30; number of baseline acquisitions before contrast agent injection = 10–15; number of time points = 120; and acquisition time ≈ and approximately 4 min.

2.3. Postprocessing of MRI data

All CEST-SAGE-EPI data were corrected for motion using rigid transformation (*mcflirt*; Functional Magnetic Resonance Imaging of the Brain Software Library, Oxford,UK; http://www.fmrib.ox.ac.uk/fsl/) and corrected for B_0 inhomogeneities using a z-spectra based k-means clustering and Lorentzian fitting algorithm (Yao et al., 2018). Then, the integral of a width of 0.4 ppm was calculated around both the − 3.0 and + 3.0 ppm spectral points (−3.2 to − 2.8 ppm and + 2.8 to + 3.2 ppm, respectively). They were coupled with the corresponding S_0 image to quantify the asymmetry in the magnetization transfer ratio (MTR_{asym}) at 3.0 ppm, a measure related to pH (Harris et al., 2016), as defined by the following equation: $MTR_{asym}(3.0\ ppm) = S(-3.0\ ppm)/S_0 - S(+3.0\ ppm)/S_0$, where S(ω) is the signal of bulk water available after the saturation pulse with offset frequency ω and S_0 is the signal available without application of saturation pulse. The first and second gradient echoes were averaged for the MTR_{asym} at 3.0 ppm to augment the available signal-to-noise. Calculation of R_2' ($=R_2^* - R_2$) was performed by solving a set of Bloch equations as previously described (Harris et al., 2018).

The dynamic time-series images of DSC MRI data were motion-corrected using *mcflirt*. Then, normalized relative CBV (nrCBV) was calculated using a leakage correction algorithm that accounts for bidirectional contrast agent exchange (Leu et al., 2016) and normalizing the CBV to the normal-appearing white matter tissue contralateral to the glioma. Creation of MTR_{asym}, R_2', and nrCBV maps were performed with MatLab (release 2017b, MathWorks) using in-house programs. All resulting maps were registered to three-dimensional post-contrast T1-weighted images for subsequent analyses (*tkregister2*; Freesurfer; Massachusetts General Hospital, Harvard Medical School; https://surfer.nmr.mgh.harvard.edu).

rOEF map was calculated by dividing R_2' by nrCBV as described previously (Toth et al., 2013). R2′ is the transverse relaxation due to local magnetic field inhomogeneities in a blood vessel network with a venous fraction of ≈0.75 × CBV (Yablonskiy et al., 2013). Assuming fully oxygenated arterial blood, the fraction of deoxygenated blood (1 − *Y*) corresponds to the OEF:

$$OEF = 1 - Y = \frac{R2'}{0.75CBV \bullet \gamma \bullet \frac{4\pi}{3} \bullet \Delta\chi_0 \bullet \mathrm{Hct} \bullet B_0}$$

In this equation, $\gamma = 2.675 \times 10^8\ s^{-1}\ T^{-1}$ is the gyromagnetic ratio, $\Delta\chi_0 = 0.264 \cdot \times\ 10^{-6}$ is the susceptibility difference between fully deoxygenated and fully oxygenated blood (Spees et al., 2001), Hct = 0.35 is the small vessel hematocrit (Silvennoinen et al., 2003), and B_0 is the magnetic field strength. Then, relative measurement of OEF can be expressed as

$$rOEF = \frac{R2'}{nrCBV}$$

AGI was calculated by dividing MTR_{asym} at 3.0 ppm by rOEF, under the assumption that aerobic glycolysis is reflected by production of lactate under inefficient use of oxygen. In equation, AGI was calculated as:

$$AGI = \frac{MTR_{asym}at3.0ppm}{rOEF} = \frac{MTR_{asym}at3.0ppm \times nrCBV}{R2'}$$

2.4. ^{18}F-FDG PET imaging (Study II)

All subjects in Study II underwent ^{18}F-FDG PET imaging on the same day as the CEST imaging. ^{18}F-FDG was synthesized using standard methods (Hamacher et al., 1986; Yu, 2006) to an average specific radioactivity of 200 GBq/mmol. After a minimum fasting period of 6 h, PET data were acquired for 15 min on PET/CT scanners (Biograph64-mCT or Biograph TruePoint, Siemens Healthcare, Erlangen, Germany) in 3D mode, 90 min after intravenous administration of ^{18}F-FDG (5 mCi). The voxel size of FDG-PET imaging was 1.6 mm × 1.6 mm × 1.5 mm or 1.34 mm × 1.3 m × 1.5 mm. Also, CT imaging was performed and reconstructed using a standard filtered back projection algorithm to correct for photon attenuation of PET data.

PET images were then registered to the post-contrast T1-weighted images using 12-degree of freedom affine registration transformation with a normalized mutual information cost function (*flirt*; Functional Magnetic Resonance Imaging of the Brain Software Library). Uptake levels of ^{18}F-FDG were normalized to the normal-appearing white matter tissue contralateral to the glioma to mitigate intersubject variability, resulting in normalized FDG (nFDG) maps (Ellingson et al., 2020).

2.5. Biopsy acquistion and immunohistochemistry (Study III)

Prospective biopsy targets were identified prior to surgery. Specifically, two to four MRI targets as spheres of 5 mm diameter were selected for each patient. These targets were selected based on the MTR_{asym} at 3.0 ppm and R_2' maps in regions with high/low acidity and high/low hypoxia. Biopsy targets were uploaded to intraoperative navigation software (Brainlab, Munich, Germany). Standard of care tumor resection was carried out with acquisition tissue corresponding to biopsy targets using intraoperative neuronavigation guidance.

Immunohistochemistry analysis was performed on 5 μm formalin-fixed, paraffin-embedded tissue sections with a customizable immunohistochemistry detection system. This all-in-one detection system contained Antigen Retrieval Stock Solution (100x), Antibody Diluent, Peroxidase Block, Protein Block, Horseradish Peroxidase Polymer - Conjugated Secondary Antibody, DAB Chromogen, DAB Substrate Buffer, and Hematoxylin and Bluing Solution. Heat-induced antigen retrieval was accomplished with Antigen Retrieval Buffer (pH 6.0) in a Decloaking Chamber at 95℃ for 30 min (Biocare Medical, Concord, CA, USA). Then, tissue sections were treated with Peroxidase Block and with Protein Block to reduce nonspecific background staining. Primary antibodies for HIF1 α (Sigma/Aldrich, HPA001275, 1:200), GLTU3 (Sigma-Aldrich, HPA006539, 1:200), hexokinase 2 (Sigma-Aldrich, HPA028587, 1:100), monocarboxylate transporter 1 (Sigma-Aldrich, SAB2702323, 1:200), lactate dehydrogenase A (Abcam, Ab47010, 1:500), and Ki67 (Sigma/Aldrich, 275R-15, 1:100) were applied for 60 min followed by detection with Horseradish Peroxidase Polymer Conjugated Secondary Antibody (anti-Rabbit or anti-Mouse). Subsequent immunodetection was completed using DAB Chromogen and counterstained with Hematoxylin and Bluing Solution. Tissue slides were scanned on a digital slide scanner (Aperio CS2; Aperio Technologies). The percentage of positive cells was calculated as the ratio of the number of positive cells to total cells in a tissue section, using semi-automated positive cell detection algorithm implemented in QuPath ver. 0.2.0-m8 (https://qupath.github.io/) (Bankhead et al., 2017).

2.6. Analysis of in vitro cellular metabolism (Study IV)

MRI-guided tissue biopsy of the contrast-enhancing region of a high-grade glioma using intraoperative image guidance was performed prior to surgical resection. Tumor cells from each sample (one cluster per each subject) were isolated as previously described (Nathanson et al., 2014). Briefly, ≈0.5 g of tumor tissue was digested via mechanical and enzymatic digestion (collagenase/DNAse), strained through a 70-μm filter, then further processed through myelin depletion by Myelin Removal Beads II (Miltenyi Biotec GmbH, Bergisch Gladbach, Germany), followed by CD45 + leukocyte depletion using CD45 MicroBeads human (Miltenyi Biotec GmbH) and red blood cell lysis. Dead cells were removed via the Dead Cell Removal Kit (Miltenyi Biotec GmbH), yielding ≈5.0 × 106 viable tumor cells/g tissue. After isolation, tumor cells were maintained as serum-free sphere cultures (gliomasphere) (Laks et al., 2016). Non-adherent gliomaspheres were dissociated, counted, and acutely attached to 25 μg/mL of Cell-Tak (Corning, New

York, NY, USA) treated Seahorse assay plate via centrifugation (600 *g* for 5 min). Then, an Agilent Seahorse XF Analyzer (Agilent Technologies, Santa Clara, CA) was used to measure rates of oxygen consumption (OCR) and extracellular acidification (ECAR)(Divakaruni et al., 2014). Basal OCR was calculated by subtracting the rate insensitive to the electron transport chain inhibitors rotenone and antimycin A, and normalized to number of cells. Adenosine triphosphate production via oxidative phosphorylation and glycolysis were also estimated from OCR and ECAR, respectively (Divakaruni et al., 2014). This was done by correcting ECAR for respiratory acidification and applying established stoichiometry. Additional experimental details and considerations for adenosine triphosphate estimation are described elsewhere (Divakaruni et al., 2014). The fraction of adenosine triphosphate derived from glycolysis to the total adenosine triphosphate was calculated and termed as cellular AGI.

2.7. Region-of-interest analysis

For imaging data of subjects in Study I and II, three mutually exclusive regions-of-interest (ROIs) were defined using a semi-automated thresholding method (Ellingson et al., 2014). They included (a) contrast-enhancing tumor and (b) central necrosis defined by T1-weighted digital subtraction maps; and (c) T2 hyperintense regions on T2-weighted FLAIR images (non-enhancing tumor), excluding areas of contrast enhancement and necrosis. Contrast-enhancing tumor + non-enhancing tumor, contrast-enhancing tumor, and non-enhancing tumor ROIs were created from these ROIs. Normal-appearing white matter ROI contralateral to the glioma was additionally created for patients in Study II, by manually delineating frontal and paietal white matter. Further, we segmented the brain of patients in Study II using SPM12 software (Wellcome Department of Imaging Neuroscience, University College London, London, UK; http://www.fil.ion.ucl.ac.uk/spm), added the gray and white matter masks to created brain masks and thresholed them at 0.9, added contrast-enhancing tumor + non-enhancing tumor masks to the brain masks, and finally binarized them to create the whole brain ROI. For analyzing data of subjects in Study III and IV, MRI targets for biopsy and contrast-enhancing tumor ROIs, respectively, were used as ROIs. These ROIs were used to retrieve median AGI and nFDG.

2.8. Statistical analysis

For patients in Study I, median AGI between IDH mutant and wild-type, and between low and high grade (i.e. grade II vs III and IV) was compared by using Mann–Whitney *U* test. AGI between contrast-enhancing tumor, non-enhancing tumor, and normal-appearing white matter was also compared only among gliomas with contrast-enhancing tumor using Kruskal-Wallis test with post-hoc Tukey's Honest Significant Difference test. Spearman's rank order correlation analysis was performed to investigate the correlation between AGI and nFDG of contrast-enhancing tumor + non-enhancing tumor, contrast-enhancing tumor, non-enhancing tumor, or the whole brain ROIs for subjects in Study II, AGI and quantitative immunohistochemistry measurements for subjects in Study III, and AGI and cellular AGI measured by bioenergetics analysis for subjects in Study IV. Confidence intervals of Spearman's ρ correlation coefficients were determined by percentile bootstrapping. The absolute values of Spearman's ρ correlation coefficients were classified as follows: 0–0.30, very weak; 0.30–0.50, weak; 0.50–0.70, moderate; 0.70–0.90, strong; and 0.90–1.00, very strong. A 2-sided P value$<$0.05 was considered statistically significant. Correction for multiple correlation analyses was not performed, to prevent overly conservative false negative detection rates considering the small sample sizes. All statistical analyses were performed by using MatLab or GraphPad Prism (Version 8.4.2; GraphPad Software, La Jolla, CA).

3. Results

3.1. Comparison of AGI between different tumor and tissue types

Figure 2 shows imaging findings of three representative cases that showed high, medium, and low AGI, and high and low ^{18}F-FDG uptake. Fig. 3 shows comparison of AGI between different tumor and tissue types. AGI was significantly lower in IDH mutant than IDH wild-type gliomas (mean ± standard deviation, 0.48 ± 0.48 vs. 0.70 ± 0.48; $P = 0.03$), and significantly lower in low-grade than high-grade gliomas (mean ± standard deviation, 0.34 ± 0.27 vs. 0.70 ± 0.54; $P = 0.01$). When compared across different tissue types, AGI was the highest in contrast-enhancing tumor, followed by non-enhancing tumor and normal-appearing white matter (mean ± standard deviation, 1.25 ± 0.72 vs. 0.41 ± 0.36 vs. 0.08 ± 0.05; all post-hoc *P-values* < 0.05).

3.2. Correlation between MR metrics and ^{18}F-FDG PET in IDH Wild-type glioblastoma

Figure 4 shows the scatterplots for comparison between AGI and nFDG. In comparison between AGI and nFDG, strong statistically significant correlations were observed in contrast-enhancing tumor + non-enhancing tumor region (ρ = 0.81; 95% CI 0.21–1.00; $P = 0.01$), non-enhancing tumor region (ρ = 0.81; 95%CI 0.32–1.00; $P = 0.01$), and contrast-enhancing tumor region (ρ = 0.81; 95% CI 0.10–1.00; $P = 0.01$). No significant correlation was found in the whole brain (ρ = − 0.62; 95% CI − 1.00–0.20; $P = 0.12$).

3.3. Correlation between MR metrics and immunohistochemistry measurements in WHO grade II–IV diffuse gliomas

Figure 5 shows examples of MRI-based biopsy targets along with corresponding MR image and AGI map, and glucose transporter 3, hexokinase 2, or monocarboxylate transporter 1 expression within these areas. Fig. 6 shows the correlation matrix for comparison between AGI and immunohistochemistry measurements and the scatterplots of AGI compared with glucose transporter 3, hexokinase 2, and monocarboxylate transporter 1. The scatterplots of all comparisons are shown in Supplementary Material (Fig. S1). Strong significant correlations were found between AGI and glucose transporter 3 (ρ = 0.71; 95% CI 0.30–0.90 ; $P = 0.006$) or hexokinase 2 (ρ = 0.73; 95% CI 0.41–0.90; $P = 0.004$) in IDH wild-type glioma. In contrast, moderate significant correlation was found between AGI and monocarboxylate transporter 1 (ρ = 0.59; 95% CI 0.19–0.74 ; $P = 0.01$) in IDH mutant glioma. No significant correlation was found between AGI and HIF1 α, lactate dehydrogenase A, or Ki-67.

3.4. Correlation between MR metrics and cellular metabolism in High-Grade glioma

Figure 7 shows imaging findings of two representative cases that showed high and low AGI, respectively, along with measurements by extracellular flux bioenergetic analysis. Fig. 8 shows the scatterplot of AGI derived from MRI compared with cellular AGI. A strong significant correlation was found between AGI and cellular AGI (ρ = 0.79; 95% CI 0.06–1.00; $P = 0.04$).

4. Discussion

The current study suggests aerobic glycolytic imaging derived from pH-, O_2–, and perfusion-weighted MRI can provide non-invasive information about the metabolic status of human diffuse gliomas. When comparing between IDH mutant and wild-type and between low- and high-grade gliomas, AGI was higher in IDH wild-type and high-grade gliomas than IDH mutant and low-grade gliomas, respectively. These observations are in line with the fact that IDH wild-type and high-grade

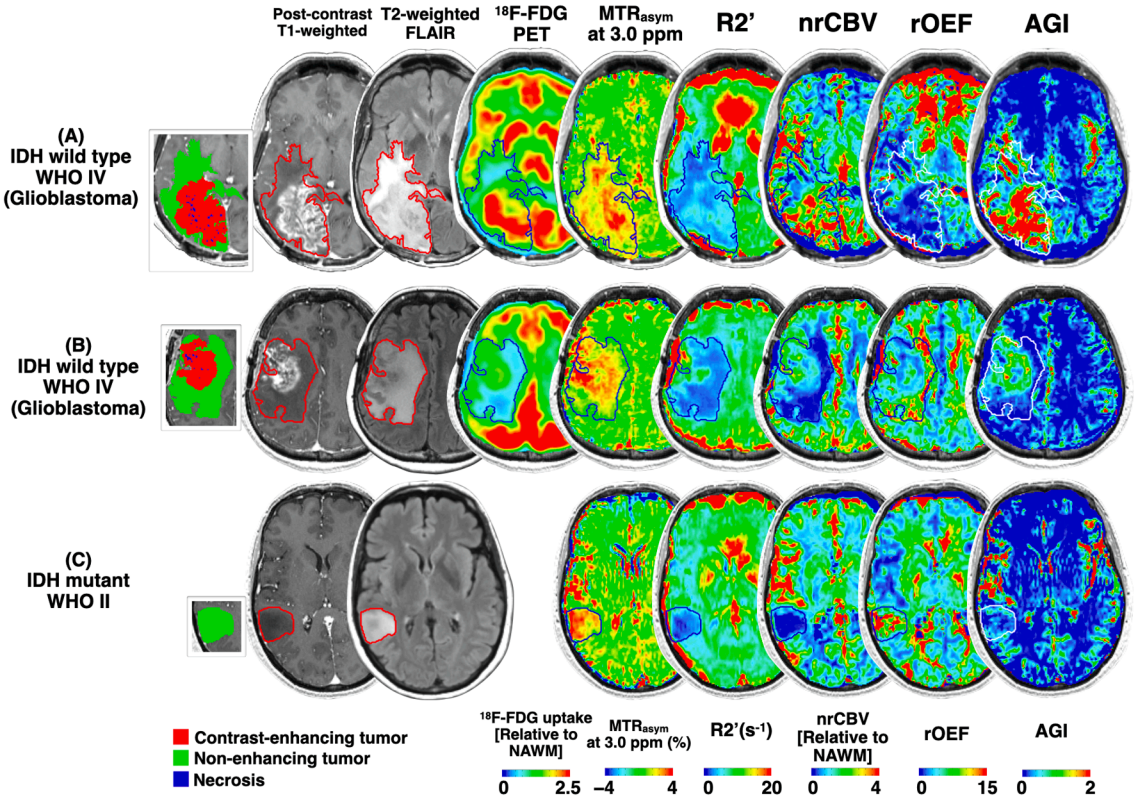

Fig. 2. Patients with diffuse gliomas with high (A, from Study II), medium (B, from Study II), and low AGI (C, from Study I), and high (A) and low (B) ^{18}F-FDG uptake. IDH wild-type glioblastomas (A and B) show higher AGI than IDH mutant grade II glioma (C). Contrast-enhancing region of the tumor is showing higher AGI than non-contrast-enhancing region of the tumor (A and B). MTR_{asym} at 3.0 ppm is grossly high in the entire tumors for both glioblastomas, while AGI seems to be correlated more with ^{18}F-FDG PET than MTR_{asym} at 3.0 ppm. While ^{18}F-FDG PET shows high physiological uptake in the cortex, quantitative maps, including AGI, derived from MRI do not show high values in the cortex. NAWM = normal-appearing white matter.

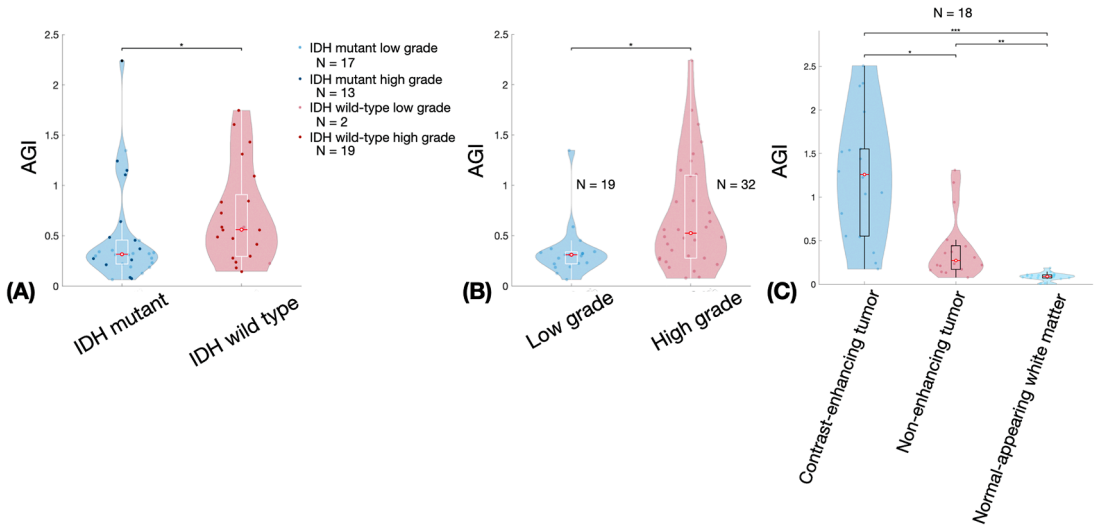

Fig. 3. Comparison of AGI between different tumor and tissue types. Box plots are overlaid on violin plots. (A) Comparison between IDH mutant and wild type. Among IDH mutant gliomas, those with AGI greater than 1 are mostly high grade (4 out of 5). (B) Comparison between low-grade and high-grade gliomas. (C) Comparison across contrast-enhancing tumor, non-enhancing tumor, and normal-appearing white matter. * $P < 0.05$, ** $P < 0.01$ *** $P < 0.001$.

gliomas have typical Warburg phenotypes, whereas IDH mutant and low-grade gliomas are more dependent on oxydative phosphorylation (Khurshed et al., 2017; Poteet et al., 2013). Further, contrast-enhancing tumor and non-enhancing tumor showed higher AGI than normal-appearing white matter, with contrast-enhancing tumor showing higher AGI than non-enhancing tumor. This may reflect the generally higher malignant status of contrast-enhancing tumor with a higher glycolytic activity than non-enhancing tumor.

Through careful metabolic investigation in Study II, we observed a strong correlation between the AGI and normalized ^{18}F-FDG PET uptake in both enhancing and non-enhancing tumor in glioblastoma, while no significant correlation was found in the whole brain. While ^{18}F-FDG PET

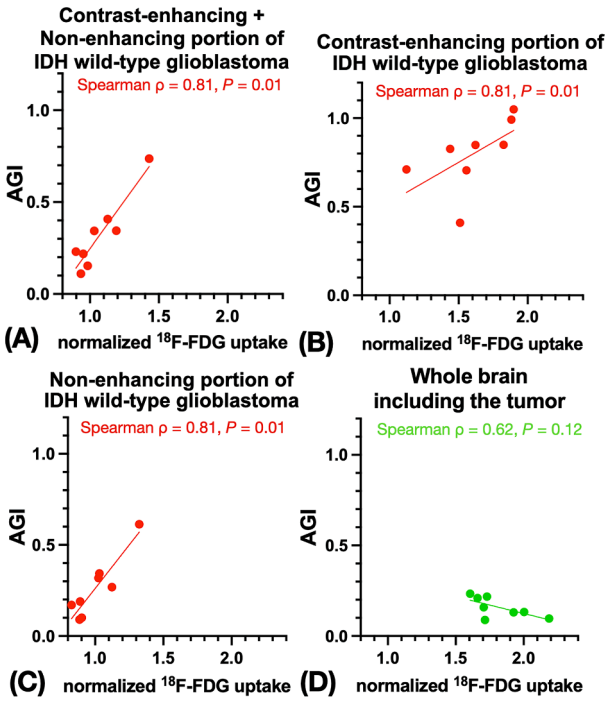

Fig. 4. Scatterplots of AGI compared with normalized ^{18}F-FDG in the contrast-enhancing plus non-enhancing (A), contrast-enhancing (B), and non-enhancing (C) portions of IDH wild-type glioblastoma and (D) the whole brain. Lines show linear regression fit to the data. Strong correlations were found in all tumor areas, while no significant correlation was found in the whole brain.

is useful for assessing response of solid tumors in other organs, its utility is limited in the brain partly due to high physiological uptake of ^{18}F-FDG in the normal brain. Because AGI exploits aspects of *abnormal* metabolism, it does not show high value in normal brain structures and therefore may be useful for both disease detection and treatment monitoring. Further, anatomical resolution is higher for AGI than ^{18}F-FDG PET. AGI may enable us to differentiate radiation necrosis from true progression, with potentially better sensitivity than ^{18}F-FDG PET due to small background AGI value (Hustinx et al., 2005). AGI may also have an indication for assessing treatment response likewise ^{18}F-FDG PET (Verger and Langen, 2017), with its ability to capture abnormal tumor metabolism. Notably, *gluco*-CEST and *gluco*-chemical exchange sensitive Spin-Lock (CESL) that have been applied in glioma also do not exhibit high background signal (Paech et al., 2017; Schuenke et al., 2017; Xu et al., 2015). However, it is expected that these approaches primarily reflect perfusion and blood–brain barrier, similarly to conventional contrast agents.

In regard to association with immunohistochemistry expression measurements, AGI showed strong significant correlation with glucose transporter 3 and hexokinase 2 in IDH wild-type glioma, while these correlations were not significant for IDH mutant glioma. Interestingly, AGI showed a moderate correlation with monocarboxylate transporter 1 in IDH mutant glioma, while this correlation was not significant for IDH wild-type glioma. These results suggest that glucose transporter 3 and hexokinase 2, which are engaged in irreversible uptake of glucose by tumor cell (Venneti and Thompson, 2017), are likely the rate-limiting factors of aerobic glycolysis in IDH wild-type glioma, in which a larger fraction of glucose is shunted to glycolysis instead of oxidative phosphorylation. On the other hand, monocarboxylate transporter, which exports lactate (the end-product of glycolysis) from the cells into the extracellular space (Yu et al., 2016), is downregulated in IDH mutant glioma (Viswanath et al., 2016) and may modulate the rate of aerobic glycolysis in IDH mutant gliomas. This is consistent with recent studies implicating lower monocarboxylate transporter expression as a major contributor to lower lactate production in immortalized IDH mutant astrocytes (Viswanath et al., 2016).

Consistent with the hypothesis that AGI derived from pH-, O_2–, and perfusion-weighted MRI reflects the degree of aerobic glycolysis specific to the underlying tumor tissue, we found strong and significant correlation between AGI and the degree of aerobic glycolysis quantified using extracellular flux bioenergetic analysis in purified tumor obtained after resection. Even though the degree of aerobic glycolysis derived from both MRI and extracellular flux analysis aim to estimate the glycolytic status, caution should be paid to the fact that their theoretical underpinnings are different. Specifically, cellular measures directly reflect adenosine triphosphate production per cell per minute, while MRI measurements are averaged over a large volume of tumor tissue. How the distribution of cells with differing metabolic features within the tumor influence MRI measures remains to be fully investigated.

There are other metabolic imaging approaches, such as ^{15}O PET and ^{17}O MRI (Fan et al., 2020; Zhu and Chen, 2017), which can potentially capture Warburg effect of gliomas. For example, ^{17}O MRI has detected decreased oxygen consumption in gliomas, presumably related to Warburg effect (Paech et al., 2020). The results of the current study warrant investigation of correlation of AGI with ^{15}O PET or ^{17}O MRI.

This study has a number of limitations. First, as mentioned above, the sample size for each experiment was small and MR acquisitions were performed on two different scanners. However, despite these sources of variability, results appeared to support the general hypothesis that aerobic glycolytic imaging derived from pH-, O_2–, and perfusion-weighted MRI reflects the general glycolytic status of the underlying tumor tissue. Second, AGI is a semi-quantitative approach and should not be considered as an absolute measurement of aerobic glycolysis. MTR_{asym} at 3.0 ppm and rOEF used for calculating AGI are both semi-quantiative measurements. Further, even though MTR_{asym} at 3.0 ppm is sensitive to tissue pH, it is not necessarily in a linear relationship with lactate concentration. Our approach may be oversimplified, and a more sophisticated approach could be more appropriate and needs to be explored in the future. Third, since AGI requires separate sets of image acquisitions (i.e. CEST-SAGE-EPI and DSC perfusion imaging), there may be some contamination from minor mis-registration, which could be problematic in evaluating small tumors or tumors residing in areas harboring large susceptibility-induced artifacts (Hagiwara et al., 2020). Fourth, even though a strong correlation was found between AGI and metrics related to glucose metabolism, AGI can also be affected by mechanisms unrelated to glucose metabolism. For example, MTR_{asym} at 3.0 ppm increases with increase in glutamine, which is consumed at a higher rate in malignant tumors (Harris et al., 2015). Correlation of AGI with abnormal glucose metabolism should be further investigated in future studies in diverse conditions. Lastly, the current study did not take into consideration the metabolic demand of immune cells that might be present *in vivo* within tumor tissue. Activated effector T cells also exhibit aerobic glycolysis, though the precise function in T cells is incompletely understood (Salmond, 2018). While results from the current study suggest AGI might be specific to abnormal metabolism from tumor cells, the influence of immune cell metabolism on AGI needs to be fully investigated, particularly if it is to be used in the context of immunotherapy.

In conclusion, aerobic glycolytic imaging showed a strong correlation with ^{18}F-FDG uptake and the degree of aerobic glycolysis of purified tumor cells using bioenergetic analysis. Aerobic glycolytic imaging correlated with key metabolic enzymes as measured with immunohistochemistry, although there were distinct differences in these associations for IDH mutant compared to wild-type gliomas, perhaps due to particular rate limiting enzymes specific to the glioma genotype. Future studies are needed to investigate the utility of aerobic glycolytic imaging for both diagnosis and treatment monitoring.

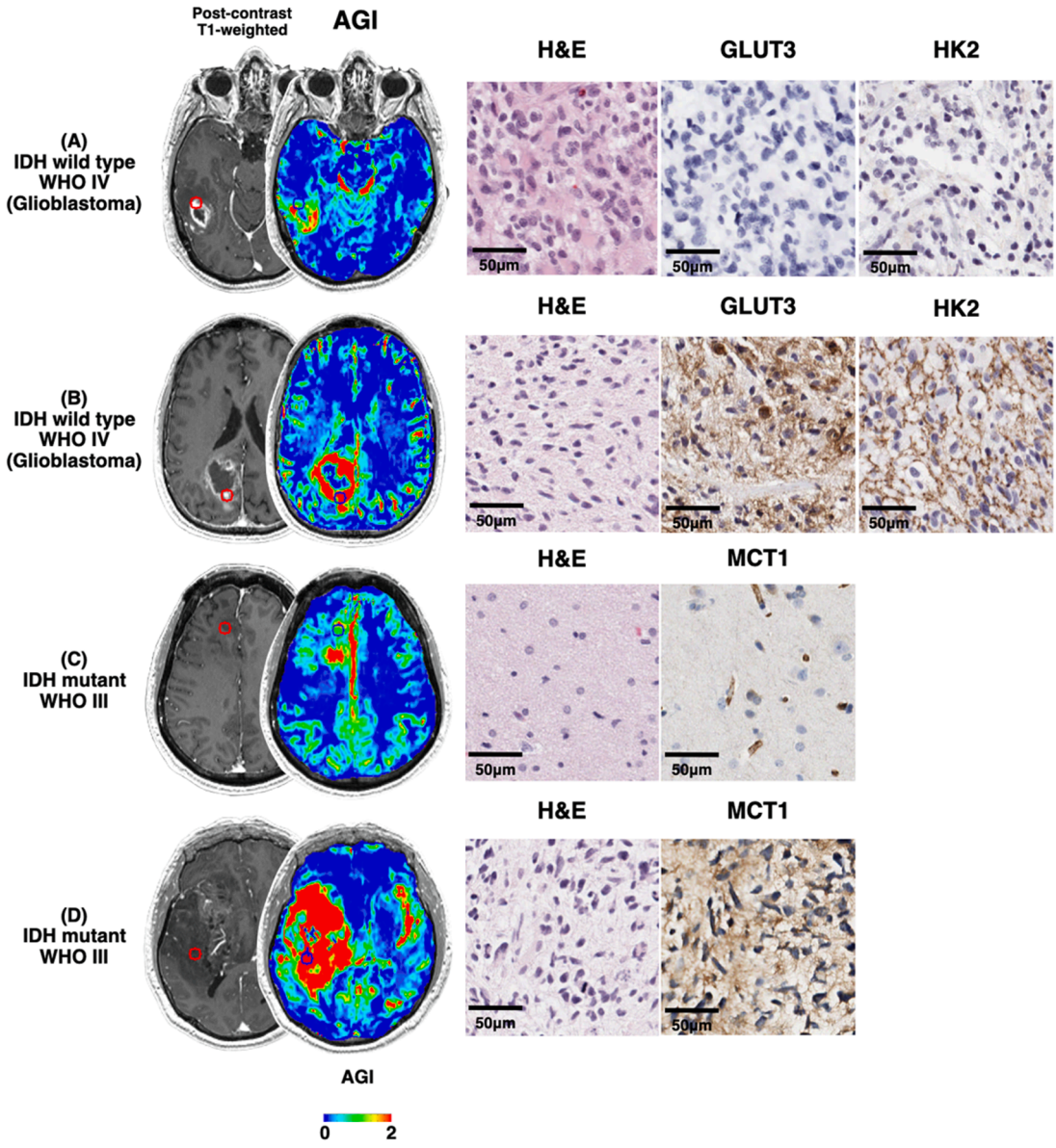

Fig. 5. MR image and AGI map and corresponding H&E and immunohistochemistry staining for MRI-guided biopsy targets (circles). (A) Treatment-naïve IDH wild-type glioblastoma for which an area with low AGI was biopsied. Expressions of GLUT3 and HK2 are low in the slides from a 5-mm radius sample taken from the MRI-guided biopsy target. (B) Treatment naïve IDH wild-type glioblastoma for which an area with high AGI was biopsied. Expressions of GLUT3 and HK2 are high. (C) Post-surgical, chemoradiotherapy-naïve IDH mutant WHO grade III glioma for which an area with low AGI was biopsied. Expression of MCT1 is low. (D) Treatment-naïve IDH mutant WHO grade III glioma for which an area with high AGI was biopsied. Expression of MCT1 is high. For GLUT3, HK2, and MCT1 stains, cells positive for expression are brown. GLUT3 = glucose transporter 3, HK2 = hexokinase 2, MCT1 = monocarboxylate transporter 1.

Funding

This work was supported by American Cancer Society (ACS) Research Scholar Grant (RSG-15–003-01-CCE) (BME); University of California Research Coordinating Committee (BME); UCLA Jonsson Comprehensive Cancer Center Seed Grant (BME); UCLA SPORE in Brain Cancer (NIH/NCI 1P50CA211015-01A1) (BME, LML, PLN, AL, WBP, TFC); NIH/NCI 1R21CA223757-01 (BME); NIH-NIGMS Training Grant GM008042 (NSC); and American Brain Tumor Association Grant Jack & Fay Netchin Medical Student Summer Fellowship supported by BrainUp MSSF2100033 (NSC).

CRediT authorship contribution statement

Akifumi Hagiwara: Data curation, Formal analysis, Visualization, Writing – original draft. **Jingwen Yao:** Data curation, Formal analysis, Writing – review & editing. **Catalina Raymond:** Data curation, Writing – review & editing. **Nicholas S. Cho:** Investigation, Writing – review & editing. **Richard Everson:** Investigation, Writing – review & editing. **Kunal Patel:** Data curation, Writing – review & editing. **Danielle H. Morrow:** Data curation, Formal analysis, Writing – review & editing. **Brandon R. Desousa:** Investigation, Writing – review & editing. **Sergey Mareninov:** Formal analysis, Writing – review & editing. **Saewon**

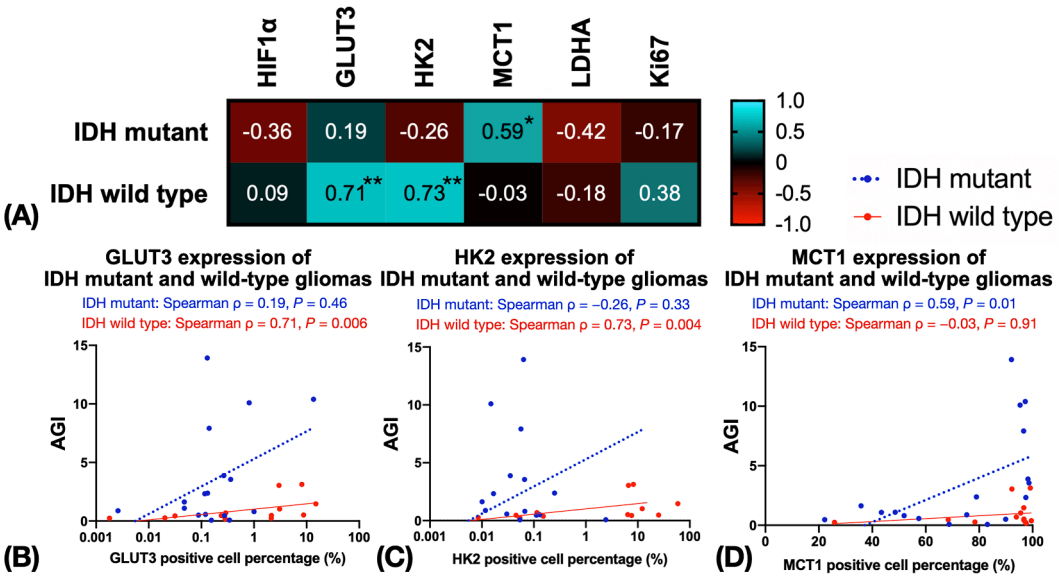

Fig. 6. (A) Correlation matrix of AGI compared with immunohistochemistry measurements shown with Spearman's correlation coefficients. * $P < 0.05$, ** $P < 0.01$. Scatterplots of AGI compared with immunohistochemistry measurement of GLUT3 (B), HK2 (C), and MCT1 (D). Lines show linear regression fit to the data. GLUT3 = glucose transporter 3; HK2 = hexokinase 2, LDHA = lactate dehydrogenase A, MCT1 = monocarboxylate transporter 1.

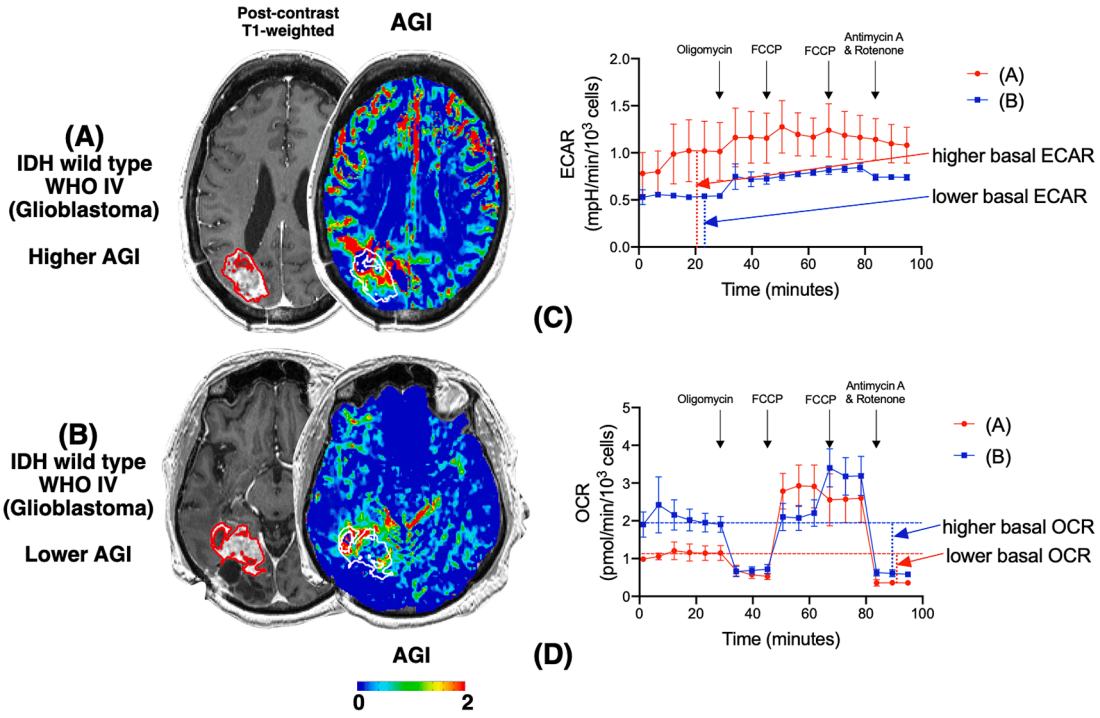

Fig. 7. MR images/maps of two patients with IDH wild-type glioblastoma that showed higher (A) and lower (B) AGI derived from MRI and extracellular flux bioenergetic analysis. An ROI of contrast-enhancing portion is overlaid on each image/map. (C), (D) Bioenergetic analysis shows higher ECAR and lower basal OCR in (A), leading to higher cellular AGI that explains higher AGI derived from MRI, whereas ECAR and OCR are lower and higher, respectively, for (B), leading to lower cellular AGI that explains lower AGI derived from MRI.

Chun: Data curation, Writing – review & editing. **David A. Nathanson:** Investigation, Writing – review & editing. **William H. Yong:** Investigation, Writing – review & editing. **Gafita Andrei:** Investigation, Writing – review & editing. **Ajit S. Divakaruni:** Investigation, Writing – review & editing. **Noriko Salamon:** Investigation, Writing – review & editing. **Whitney B. Pope:** Investigation, Writing – review & editing, Investigation, Writing – review & editing. **Phioanh L. Nghiemphu:** Investigation, Writing – review & editing. **Linda M. Liau:** Investigation, Writing – review & editing. **Timothy F. Cloughesy:** Investigation, Writing – review & editing. **Benjamin M. Ellingson:** Conceptualization, Visualization, Writing – review & editing.

Declaration of Competing Interest

The authors declare the following financial interests/personal relationships which may be considered as potential competing interests:

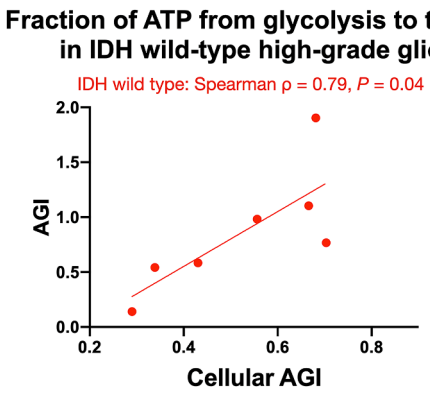

Fig. 8. Scatterplot of AGI compared with cellular AGI derived from bioenergetic extracellular flux analysis. Lines show linear regression fit to the data. A strong correlation was found between AGI and cellular AGI.

ASD has previously served as a paid consultant to Agilent Technologies. BME is on advisory board of Hoffman La-Roche, Siemens, Nativis, Medicenna, MedQIA, Bristol Meyers Squibb, Imaging Endpoints, and Agios. BME is a paid consultant of Nativis, MedQIA, Siemens, Hoffman La-Roche, Imaging Endpoints, Medicenna, and Agios. BME has grant funding by Hoffman La-Roche, Siemens, Agios, and Janssen. BME holds a patent on this technology (US Patent #15/577664; International PCT/US2016/034886).

Appendix A. Supplementary data

Supplementary data to this article can be found online at https://doi.org/10.1016/j.nicl.2021.102882.

References

Atkinson, I.C., Thulborn, K.R., 2010. Feasibility of mapping the tissue mass corrected bioscale of cerebral metabolic rate of oxygen consumption using 17-oxygen and 23-sodium MR imaging in a human brain at 9.4 T. Neuroimage 51 (2), 723–733.

Bankhead, P., Loughrey, M.B., Fernandez, J.A., Dombrowski, Y., McArt, D.G., Dunne, P. D., McQuaid, S., Gray, R.T., Murray, L.J., Coleman, H.G., James, J.A., Salto-Tellez, M., Hamilton, P.W., 2017. QuPath: Open source software for digital pathology image analysis. Sci. Rep. 7, 16878.

Brat, D.J., Castellano-Sanchez, A.A., Hunter, S.B., Pecot, M., Cohen, C., Hammond, E.H., Devi, S.N., Kaur, B., Van Meir, E.G., 2004. Pseudopalisades in glioblastoma are hypoxic, express extracellular matrix proteases, and are formed by an actively migrating cell population. Cancer Res. 64 (3), 920–927.

Chesnelong, C., Chaumeil, M.M., Blough, M.D., Al-Najjar, M., Stechishin, O.D., Chan, J. A., Pieper, R.O., Ronen, S.M., Weiss, S., Luchman, H.A., Cairncross, J.G., 2014. Lactate dehydrogenase A silencing in IDH mutant gliomas. Neuro Oncol 16, 686-695.

Corbet, C., Feron, O., 2017. Tumour acidosis: from the passenger to the driver's seat. Nat. Rev. Cancer 17 (10), 577–593.

Divakaruni, A.S., Paradyse, A., Ferrick, D.A., Murphy, A.N., Jastroch, M., 2014. Analysis and interpretation of microplate-based oxygen consumption and pH data. Methods Enzymol. 547, 309–354.

Ellingson, B.M., Bendszus, M., Boxerman, J., Barboriak, D., Erickson, B.J., Smits, M., Nelson, S.J., Gerstner, E., Alexander, B., Goldmacher, G., Wick, W., Vogelbaum, M., Weller, M., Galanis, E., Kalpathy-Cramer, J., Shankar, L., Jacobs, P., Pope, W.B., Yang, D., Chung, C., Knopp, M.V., Cha, S., van den Bent, M.J., Chang, S., Yung, W.K., Cloughesy, T.F., Wen, P.Y., Gilbert, M.R., Jumpstarting Brain Tumor Drug Development Coalition Imaging Standardization Steering, C., 2015. Consensus recommendations for a standardized Brain Tumor Imaging Protocol in clinical trials. Neuro Oncol. 17, 1188–1198.

Ellingson, B.M., Kim, H.J., Woodworth, D.C., Pope, W.B., Cloughesy, J.N., Harris, R.J., Lai, A., Nghiemphu, P.L., Cloughesy, T.F., 2014. Recurrent glioblastoma treated with bevacizumab: contrast-enhanced T1-weighted subtraction maps improve tumor delineation and aid prediction of survival in a multicenter clinical trial. Radiology 271 (1), 200–210.

Ellingson, B.M., Yao, J., Raymond, C., Nathanson, D.A., Chakhoyan, A., Simpson, J., Garner, J.S., Olivero, A.G., Mueller, L.U., Rodon, J., Gerstner, E., Cloughesy, T.F., Wen, P.Y., 2020. Multi-parametric MR-PET imaging predicts pharmacokinetics and clinical response to GDC-0084 in patients with recurrent high-grade glioma. Clin. Cancer Res. 26 (13), 3135–3144.

Fan, A.P., An, H., Moradi, F., Rosenberg, J., Ishii, Y., Nariai, T., Okazawa, H., Zaharchuk, G., 2020. Quantification of brain oxygen extraction and metabolism with [(15)O]-gas PET: A technical review in the era of PET/MRI. Neuroimage 220, 117136. https://doi.org/10.1016/j.neuroimage.2020.117136.

Fujita, N., Shinohara, M., Tanaka, H., Yutani, K., Nakamura, H., Murase, K., 2003. Quantitative mapping of cerebral deoxyhemoglobin content using MR imaging. Neuroimage 20, 2071–2083.

Gatenby, R.A., Gillies, R.J., 2004. Why do cancers have high aerobic glycolysis? Nat. Rev. Cancer 4 (11), 891–899.

Hagiwara, A., Fujita, S., Ohno, Y., Aoki, S., 2020. Variability and Standardization of Quantitative Imaging: Monoparametric to Multiparametric Quantification, Radiomics, and Artificial Intelligence. Invest. Radiol. 55 (9), 601–616.

Hamacher, K., Coenen, H.H., Stocklin, G., 1986. Efficient stereospecific synthesis of no-carrier-added 2-[18F]-fluoro-2-deoxy-D-glucose using aminopolyether supported nucleophilic substitution. J. Nucl. Med. 27, 235–238.

Harris, R.J., Cloughesy, T.F., Liau, L.M., Nghiemphu, P.L., Lai, A., Pope, W.B., Ellingson, B.M., 2016. Simulation, phantom validation, and clinical evaluation of fast pH-weighted molecular imaging using amine chemical exchange saturation transfer echo planar imaging (CEST-EPI) in glioma at 3 T. NMR Biomed. 29, 1563–1576.

Harris, R.J., Cloughesy, T.F., Liau, L.M., Prins, R.M., Antonios, J.P., Li, D., Yong, W.H., Pope, W.B., Lai, A., Nghiemphu, P.L., Ellingson, B.M., 2015. pH-weighted molecular imaging of gliomas using amine chemical exchange saturation transfer MRI. Neuro Oncol 17 (11), 1514–1524.

Harris, R.J., Yao, J., Chakhoyan, A., Raymond, C., Leu, K., Liau, L.M., Nghiemphu, P.L., Lai, A., Salamon, N., Pope, W.B., Cloughesy, T.F., Ellingson, B.M., 2018. Simultaneous pH-sensitive and oxygen-sensitive MRI of human gliomas at 3 T using multi-echo amine proton chemical exchange saturation transfer spin-and-gradient echo echo-planar imaging (CEST-SAGE-EPI). Magn. Reson. Med. 80, 1962–1978.

Hustinx, R., Pourdehnad, M., Kaschten, B., Alavi, A., 2005. PET imaging for differentiating recurrent brain tumor from radiation necrosis. Radiol. Clin. North Am. 43 (1), 35–47.

Khurshed, M., Molenaar, R.J., Lenting, K., Leenders, W.P., van Noorden, C.J.F., 2017. In silico gene expression analysis reveals glycolysis and acetate anaplerosis in IDH1 wild-type glioma and lactate and glutamate anaplerosis in IDH1-mutated glioma. Oncotarget 8 (30), 49165–49177.

Koivunen, P., Lee, S., Duncan, C.G., Lopez, G., Lu, G., Ramkissoon, S., Losman, J.A., Joensuu, P., Bergmann, U., Gross, S., Travins, J., Weiss, S., Looper, R., Ligon, K.L., Verhaak, R.G.W., Yan, H., Kaelin Jr, W.G., 2012. Transformation by the (R)-enantiomer of 2-hydroxyglutarate linked to EGLN activation. Nature 483 (7390), 484–488.

Lai, A., Kharbanda, S., Pope, W.B., Tran, A., Solis, O.E., Peale, F., Forrest, W.F., Pujara, K., Carrillo, J.A., Pandita, A., Ellingson, B.M., Bowers, C.W., Soriano, R.H., Schmidt, N.O., Mohan, S., Yong, W.H., Seshagiri, S., Modrusan, Z., Jiang, Z., Aldape, K.D., Mischel, P.S., Liau, L.M., Escovedo, C.J., Chen, W., Nghiemphu, P.L., James, C.D., Prados, M.D., Westphal, M., Lamszus, K., Cloughesy, T., Phillips, H.S., 2011. Evidence for sequenced molecular evolution of IDH1 mutant glioblastoma from a distinct cell of origin. J. Clin. Oncol. 29 (34), 4482–4490.

Laks, D.R., Crisman, T.J., Shih, M.Y.S., Mottahedeh, J., Gao, F., Sperry, J., Garrett, M.C., Yong, W.H., Cloughesy, T.F., Liau, L.M., Lai, A., Coppola, G., Kornblum, H.I., 2016. Large-scale assessment of the gliomasphere model system. Neuro Oncol 18 (10), 1367–1378.

Lebrun-Grandie, P., Baron, J.C., Soussaline, F., Loch'h, C., Sastre, J., Bousser, M.G., 1983. Coupling between regional blood flow and oxygen utilization in the normal human brain. A study with positron tomography and oxygen 15. Arch. Neurol. 40, 230–236.

Leu, K., Boxerman, J.L., Lai, A., Nghiemphu, P.L., Pope, W.B., Cloughesy, T.F., Ellingson, B.M., 2016. Bidirectional Contrast agent leakage correction of dynamic susceptibility contrast (DSC)-MRI improves cerebral blood volume estimation and survival prediction in recurrent glioblastoma treated with bevacizumab. J. Magn. Reson. Imaging 44 (5), 1229–1237.

Morita, T., Nagaki, T., Fukuda, I., Okumura, K., 1992. Clastogenicity of low pH to various cultured mammalian cells. Mutat. Res. 268 (2), 297–305.

Nathanson, D.A., Gini, B., Mottahedeh, J., Visnyei, K., Koga, T., Gomez, G., Eskin, A., Hwang, K., Wang, J., Masui, K., Paucar, A., Yang, H., Ohashi, M., Zhu, S., Wykosky, J., Reed, R., Nelson, S.F., Cloughesy, T.F., James, C.D., Rao, P.N., Kornblum, H.I., Heath, J.R., Cavenee, W.K., Furnari, F.B., Mischel, P.S., 2014. Targeted therapy resistance mediated by dynamic regulation of extrachromosomal mutant EGFR DNA. Science 343 (6166), 72–76.

Niesporek, S.C., Umathum, R., Lommen, J.M., Behl, N.G.R., Paech, D., Bachert, P., Ladd, M.E., Nagel, A.M., 2018. Reproducibility of CMRO2 determination using dynamic (17) O MRI. Magn. Reson. Med. 79 (6), 2923–2934.

Paech, D., Nagel, A.M., Schultheiss, M.N., Umathum, R., Regnery, S., Scherer, M., Wick, A., Platt, T., Wick, W., Bendszus, M., Unterberg, A., Schlemmer, H.-P., Ladd, M.E., Niesporek, S.C., 2020. Quantitative Dynamic Oxygen 17 MRI at 7.0 T for the Cerebral Oxygen Metabolism in Glioma. Radiology 295 (1), 181–189.

Paech, D., Schuenke, P., Koehler, C., Windschuh, J., Mundiyanapurath, S., Bickelhaupt, S., Bonekamp, D., Baumer, P., Bachert, P., Ladd, M.E., Bendszus, M., Wick, W., Unterberg, A., Schlemmer, H.P., Zaiss, M., Radbruch, A., 2017. T1rho-weighted Dynamic Glucose-enhanced MR Imaging in the Human Brain. Radiology 285, 914–922.

Poteet, E., Choudhury, G.R., Winters, A., Li, W., Ryou, M.-G., Liu, R., Tang, L., Ghorpade, A., Wen, Y., Yuan, F., Keir, S.T., Yan, H., Bigner, D.D., Simpkins, J.W., Yang, S.-H., 2013. Reversing the Warburg effect as a treatment for glioblastoma. J. Biol. Chem. 288 (13), 9153–9164.

Salmond, R.J., 2018. mTOR regulation of glycolytic metabolism in T Cells. Front. Cell Dev. Biol. 6, 122.

Schuenke, P., Paech, D., Koehler, C., Windschuh, J., Bachert, P., Ladd, M.E., Schlemmer, H.P., Radbruch, A., Zaiss, M., 2017. Fast and quantitative T1rho-weighted dynamic glucose enhanced MRI. Sci. Rep. 7, 42093.

Silvennoinen, M.J., Clingman, C.S., Golay, X., Kauppinen, R.A., van Zijl, P.C.M., 2003. Comparison of the dependence of blood R2 and R2* on oxygen saturation at 1.5 and 4.7 Tesla. Magn. Reson. Med. 49 (1), 47–60.

Spees, W.M., Yablonskiy, D.A., Oswood, M.C., Ackerman, J.J.H., 2001. Water proton MR properties of human blood at 1.5 Tesla: magnetic susceptibility, T(1), T(2), T*(2), and non-Lorentzian signal behavior. Magn. Reson. Med. 45 (4), 533–542.

Sun, P.Z., Benner, T., Copen, W.A., Sorensen, A.G., 2010. Early experience of translating pH-weighted MRI to image human subjects at 3 Tesla. Stroke 41, S147–S151.

Toth, V., Förschler, A., Hirsch, N.M., den Hollander, J., Kooijman, H., Gempt, J., Ringel, F., Schlegel, J., Zimmer, C., Preibisch, C., 2013. MR-based hypoxia measures in human glioma. J. Neurooncol. 115 (2), 197–207.

Venneti, S., Thompson, C.B., 2017. Metabolic reprogramming in brain tumors. Annu. Rev. Pathol. 12 (1), 515–545.

Verger, A., Langen, K.J., 2017. PET Imaging in Glioblastoma: Use in Clinical Practice. In: De Vleeschouwer, S. (Ed.), Glioblastoma, Brisbane (AU).

Viswanath, P., Najac, C., Izquierdo-Garcia, J.L., Pankov, A., Hong, C., Eriksson, P., Costello, J.F., Pieper, R.O., Ronen, S.M., 2016. Mutant IDH1 expression is associated with down-regulation of monocarboxylate transporters. Oncotarget 7 (23), 34942–34955.

Wu, B., Warnock, G., Zaiss, M., Lin, C., Chen, M., Zhou, Z., Mu, L., Nanz, D., Tuura, R., Delso, G., 2016. An overview of CEST MRI for non-MR physicists. EJNMMI Phys 3, 19.

Wu, M., Neilson, A., Swift, A.L., Moran, R., Tamagnine, J., Parslow, D., Armistead, S., Lemire, K., Orrell, J., Teich, J., Chomicz, S., Ferrick, D.A., 2007. Multiparameter metabolic analysis reveals a close link between attenuated mitochondrial bioenergetic function and enhanced glycolysis dependency in human tumor cells. Am. J. Physiol. Cell Physiol. 292 (1), C125–C136.

Xu, X., Yadav, N.N., Knutsson, L., Hua, J., Kalyani, R., Hall, E., Laterra, J., Blakeley, J., Strowd, R., Pomper, M., Barker, P., Chan, K.W.Y., Liu, G., McMahon, M.T., Stevens, R.D., van Zijl, P.C.M., 2015. Dynamic glucose-enhanced (DGE) MRI: translation to human scanning and first results in glioma patients. Tomography 1 (2), 105–114.

Yablonskiy, D.A., Sukstanskii, A.L., He, X., 2013. Blood oxygenation level-dependent (BOLD)-based techniques for the quantification of brain hemodynamic and metabolic properties - theoretical models and experimental approaches. NMR Biomed. 26, 963–986.

Yao, J., Chakhoyan, A., Nathanson, D.A., Yong, W.H., Salamon, N., Raymond, C., Mareninov, S., Lai, A., Nghiemphu, P.L., Prins, R.M., Pope, W.B., Everson, R.G., Liau, L.M., Cloughesy, T.F., Ellingson, B.M., 2019. Metabolic characterization of human IDH mutant and wild type gliomas using simultaneous pH- and oxygen-sensitive molecular MRI. Neuro Oncol.

Yao, J., Ruan, D., Raymond, C., Liau, L.M., Salamon, N., Pope, W.B., Nghiemphu, P.L., Lai, A., Cloughesy, T.F., Ellingson, B.M., 2018. Improving B0 correction for pH-weighted amine proton chemical exchange saturation transfer (CEST) imaging by use of k-means clustering and Lorentzian estimation. Tomography 4 (3), 123–137.

Yu, L., Chen, X., Wang, L., Chen, S., 2016. The sweet trap in tumors: aerobic glycolysis and potential targets for therapy. Oncotarget 7 (25), 38908–38926.

Yu, S., 2006. Review of F-FDG synthesis and quality control. Biomed Imaging Interv J. 2, e57.

Zhu, X.H., Chen, W., 2017. In vivo(17)O MRS imaging - Quantitative assessment of regional oxygen consumption and perfusion rates in living brain. Anal. Biochem. 529, 171–178.